Modeling the response of small myelinated axons in a compound nerve to kilohertz frequency signals

N A Pelot[1], **C E Behrend**[1], and **W M Grill**[1]

[1]Department of Biomedical Engineering, Duke University, Room 1427, Fitzpatrick CIEMAS, 101 Science Drive, Campus Box 90281, Durham, NC 27708

Abstract

Objective—There is growing interest in electrical neuromodulation of peripheral nerves, particularly autonomic nerves, to treat various diseases. Electrical signals in the kilohertz frequency (KHF) range can produce different responses, including conduction block. For example, EnteroMedics' vBloc® therapy for obesity delivers 5 kHz stimulation to block the abdominal vagus nerves, but the mechanisms of action are unclear.

Approach—We developed a two-part computational model, coupling a three-dimensional finite element model of a cuff electrode around the human abdominal vagus nerve with biophysically-realistic electrical circuit equivalent (cable) model axons (1, 2, and 5.7 μm in diameter). We developed an automated algorithm to classify conduction responses as subthreshold (transmission), KHF-evoked activity (excitation), or block. We quantified neural responses across kilohertz frequencies (5 to 20 kHz), amplitudes (1 to 8 mA), and electrode designs.

Main results—We found heterogeneous conduction responses across the modeled nerve trunk, both for a given parameter set and across parameter sets, although most suprathreshold responses were excitation, rather than block. The firing patterns were irregular near transmission and block boundaries, but otherwise regular, and mean firing rates varied with electrode-fibre distance. Further, we identified excitation responses at amplitudes above block threshold, termed "re-excitation", arising from action potentials initiated at virtual cathodes. Excitation and block thresholds decreased with smaller electrode-fibre distances, larger fibre diameters, and lower kilohertz frequencies. A point source model predicted a larger fraction of blocked fibres and greater change of threshold with distance as compared to the realistic cuff and nerve model.

Significance—Our findings of widespread asynchronous KHF-evoked activity suggest that conduction block in the abdominal vagus nerves is unlikely with current clinical parameters. Our results indicate that compound neural or downstream muscle force recordings may be unreliable as quantitative measures of neural activity for in vivo studies or as biomarkers in closed-loop clinical devices.

1. Introduction

There is growing interest in electrical neuromodulation of peripheral nerves, particularly autonomic nerves, to treat a variety of diseases [1–3]. Applications of peripheral nerve stimulation include treatment of bladder dysfunction [4], obesity [5], rheumatoid arthritis [6], heart failure [7], and type II diabetes [8]. Unlike the widespread effects of pharmaceuticals, peripheral nerve stimulation offers the advantage of precisely targeted therapy.

In particular, there is growing interest in kilohertz frequency (KHF) electrical signals that can block conduction of action potentials in nearby neurons [9]. Indeed, to achieve the precise control required to generate therapeutic patterns of neural activity, simply stimulating with conventional waveforms to elicit action potentials may not be sufficient. Rather, a full spectrum of neuromodulatory therapies also requires the capability to block pathological activity, such as with KHF electrical signals; these signals have been applied to the spinal cord to treat chronic pain [10], to peripheral somatosensory nerves to treat phantom limb pain [11], and to the abdominal vagus nerves to treat obesity [5].

EnteroMedics received FDA approval for vBloc® therapy (Vagal BLocking for Obesity Control) in January 2015 to treat obesity [12]. The therapy involves placing cuff electrodes around the anterior and posterior abdominal vagus nerves and delivering 5 kHz (90 μs phase width) electrical signals at 1 to 8 mA (typically 6 mA) for 2 to 5 min ON and 5 to 10 min OFF for 13 hours per day [13]. EnteroMedics claims that the therapy blocks hunger and gastric accommodation signals in the vagi, thereby producing weight loss [5]. However, the therapy's efficacy and mechanisms of action are controversial, particularly considering that neither the first (EMPOWER) [14] nor the second (ReCharge) clinical trial [5] met its primary efficacy endpoint.

While the effects of KHF signals on large myelinated somatic fibres have been investigated extensively through computational and in vivo studies [9], the effects of KHF electrical signals on small diameter autonomic nerve fibres is poorly understood. Quantifying the effects of KHF signals on small autonomic fibres is required for understanding the parameter space to achieve targeted and effective patterned peripheral nerve stimulation and block. Therefore, we developed a two-part computational model consistent with standard neural modeling practices [15,16], coupling a three-dimensional finite element model (FEM) with biophysically-realistic electrical circuit equivalent (cable) model axons. Unlike previous computational KHF studies which used a point source in a homogeneous isotropic extracellular medium [17–23], we represented the geometries of a compound nerve and surrounding cuff electrode. We developed an automated algorithm to classify the conduction responses to various KHF signals, and we quantified neural responses across a range of kilohertz frequencies, amplitudes, and electrode designs. Parts of this work were presented in a short conference paper [24].

2. Methods

2.1. Finite Element Model of Nerve and Electrode

We constructed a three-dimensional FEM of the abdominal vagus nerve with a monopolar cuff electrode in COMSOL Multiphysics 4.4 (COMSOL Inc., Burlington, MA) to obtain the distribution of electric potentials in the tissue (Figure 1). The electrical and geometrical parameters are presented in Table 1. The model includes 30 randomly positioned and sized fascicles, each surrounded by perineurium. We modeled the perineurium as a contact impedance boundary condition using a thin layer approximation; we validated this approach by ensuring that the cathodic excitation threshold was unchanged when modeling the perineurium with a finite thickness using a simplified model with a single fascicle (data not shown). The endoneurium was anisotropic, and we halved the radial resistivity from the value measured for cat dorsal columns [25] given that the abdominal vagi are primarily composed of unmyelinated fibres [26,27]. A sensitivity analysis on the endoneurial resistivity revealed that thresholds were only affected by the longitudinal resistivity, and not the radial value, when changed by a factor of one half to two.

We placed a model of EnteroMedics' cuff electrode [30,31] around the nerve, surrounded by encapsulation tissue (Figure 1). We held the active electrode at 1 V and integrated the current density over the electrode surface to determine the total applied current (0.185 mA). We placed the nerve and cuff in a homogeneous isotropic fatty medium with all outside surfaces grounded.

We meshed the FEM with 1,283,840 triangular prism elements; specifically, we created a 2D mesh with triangular elements on the top surface, which we then swept to the bottom surface. Using the conjugate gradients solver, we obtained the electric potentials by solving Laplace's equation:

$$\nabla \cdot (\sigma \cdot \nabla \phi) = 0 \quad (1)$$

We used cubic and quadratic shape functions to interpolate the geometry and the solution, respectively, assuming quasi-static conditions and non-dispersive materials. We verified that increasing the size of the surrounding volume or increasing the number of elements resulted in <3% change in cathodic activation thresholds for a 2 μm axon centred in each fascicle. Further, the length of the model was sufficient to avoid end excitation due to effects of the KHF signal near the terminations of the myelinated axons.

In addition to the partial cuff design shown in Figure 1, we examined the effects of electrode design by modeling a complete circumneural cuff, as well as a point source electrode in a homogeneous isotropic medium, for which we obtained the potentials using:

$$\phi = \frac{I\rho}{4\pi r} \quad (2)$$

where ρ was 5 Ω-m [18] and r was the distance from the point source to each segment in the model axon. We simulated the same 30 electrode-fibre distances as in the compound nerve FEM.

2.2. Simulations with Model Axons

Using NEURON v7.3 [38], we modeled 100 mm-long small myelinated axons (1, 2, 5.7 μm myelin diameter) based upon the MRG model of mammalian peripheral nerve fibres at 37°C [39,40]. The myelinated fibres of the abdominal vagi have myelin diameters of 1 to 8 μm in humans, with most ranging from 2 to 6 μm [41], which is similar to cats (2 to 5 μm [26]) and rats (1 to 4 μm [27]). The original MRG paper [39] presents a double-cable model of larger myelinated axons (5.7 to 16 μm diameter). To model 2 μm diameter myelinated fibres, we used the geometrical parameters in a subsequent paper [40]. We extrapolated these values to model 1 μm axons due to a lack of published data on the ultrastructure of small myelinated fibres, resulting in 15 myelin lamellae, and lengths of 1, 3, 5, and 83 μm and axonal diameters of 0.7, 0.7, 0.8, and 0.8 μm for the node of Ranvier, paranodal, juxtaparanodal, and internodal segments, respectively. The 1 and 2 μm model axons had conduction speeds of 4.0 and 8.4 m/s, respectively, consistent with measured values [42–44].

From the FEM, we extracted potentials along the axis of each fascicle to apply extracellularly at a given KHF and amplitude to a model axon of each diameter. Due to the high resistivity of the perineurium, the position of the axon within a fascicle had little effect on threshold. In addition to the KHF extracellular potentials, we applied a 100 Hz suprathreshold intracellular stimulus to a node of Ranvier 6 mm from the proximal end of the axon to evoke intrinsic activity and recorded the transmembrane potential 5 mm from the distal end. The KHF stimulation started at t = 1 ms and the intracellular test pulses began at t = 25 ms. The two end-nodes had passive (linear) membrane properties to reduce the potential for end excitation. We initialized each simulation with 10 ms time steps from t = −200 ms to t = 0 ms to ensure initial steady-state. We ran each simulation for 250 ms with 5 μs time steps using the backward Euler integration method. Shortening the time step to 1 μs or extending the simulation time to 2000 ms had insignificant effects on the results. All NEURON simulations were run on the Neuroscience Gateway computer cluster [45].

2.3. Data Analysis

We developed an automated data analysis algorithm in MATLAB R2012b (MathWorks, Inc., Natick, MA) to classify the recorded conduction responses. We ran each simulation with and without the intracellular stimulus (intrinsic activity) and KHF signal to permit identification of the source(s) of recorded action potentials.

We initially classified each spike train using eight categories of conduction responses with a progressive algorithm (if-elseif-else structure), after which the results were simplified into three categories: transmission, excitation, and block (Figure 2). The spike times were automatically identified via a rising edge passing V_m = −30 mV, and spike times were identified as equal with a tolerance of 0.5 ms.

We computed the mean firing rate (FR_{mean}) and the entropy for the responses classified as excitation. We computed the direct entropy of logarithmically-binned probability distributions of pairs of interspike intervals (ISIs) [46]:

$$H = -\frac{1}{2}\sum_{a=1}^{N}\sum_{b=1}^{N} P(ISI_a, ISI_b) * log_2 P(ISI_a, ISI_b) \quad (3)$$

The right-hand side of the kth bin used to create the probability distributions was given by:

$$bin_k = bin_0 * 10^{\frac{k}{\kappa}} \quad (4)$$

We selected $bin_0 = 0.4$ ms (smaller than the shortest ISI) and $\kappa = 20$ (number of discrete time bins per ISI decade). We defined $N = 62$ bins, where $bin_{62} = 504$ ms (larger than the longest ISI). Terms in the summation where $P = 0$ for a given (ISI_a, ISI_b) pair contributed zero to the entropy. Computing the probability distribution of pairs of ISIs rather than ISIs in isolation helps account for the dependence between pairs of spikes rather than considering them as independent events. We computed entropy for 2000 ms simulations, rather than 250 ms, since small datasets can severely bias entropy estimates [46].

3. Results

Using a computational model, we investigated the effects of KHF electrical signals delivered via a cuff electrode on small myelinated fibres in the human abdominal vagus nerve. We quantified the conduction responses through automated categorization (transmission, excitation, block), mean firing rate, and entropy. We also investigated the effects of electrode design and intrinsic firing rate. Lastly, we examined the mechanisms of block and excitation.

3.1. Conduction Responses

Figure 3 (top section) shows the base set of conduction responses, colour-coded as transmission, excitation, or block, spanning three fibre diameters (1, 2, 5.7 μm), three KHF values (5, 10, 20 kHz), and eight amplitudes (1 to 8 mA, Δ = 1 mA). We observed heterogeneous responses across the nerve, both for a given parameter set and across parameter sets. The data revealed trends analogous to those well-established for responses to a conventional cathodic pulse, i.e. higher action potential initiation thresholds for smaller diameter axons (threshold-diameter relationship) and for axons farther from the electrode (threshold-distance relationship) [47]. Axons with smaller diameters and larger electrode-fibre distances had higher KHF excitation and block thresholds, and thresholds increased with higher kilohertz frequencies, as previously described [20].

Within the tested range of amplitudes (1 to 8 mA), no block was observed for the 1 μm axons across all kilohertz frequencies or for the 2 μm axons with the 5 kHz signal. For amplitudes, frequencies, and fibre diameters that resulted in block (i.e. in a single nerve cross-section in Figure 3, top section), block occurred in distinct spatial bands approximately parallel to the partial cuff electrode, flanked by excitation in fascicles both

closer to and farther from the cuff. More generally, with smaller electrode-fibre distances, larger KHF amplitudes, larger fibre diameters, and lower kilohertz frequencies, the axonal conduction response progressed from transmission, to excitation, to block, and to excitation again ("re-excitation"), a phenomenon that has not previously been described (see below). Thus, the amplitudes that resulted in block for certain axons and KHF values may have been missed in the data presented in Figure 3; in parameter sets showing excitation (and transmission, if applicable) without block, the axons may all be in a state of excitation, or some may be excited and others re-excited for larger and smaller electrode-fibre distances, respectively.

Figure 3 presents the conduction responses using three simplified categories, but initial classification included eight categories, as defined in Figure 2, for which the results are shown in Supplemental Figure 1. Transmission categories 2 and 3 only occurred near excitation threshold. Regarding the types of excitation, category 5 (excitation due to the combination of intrinsic activity and KHF signal) was not observed, and category 6 (same as category 5 after KHF-evoked onset response) occurred infrequently and only near transmission and block boundaries. Similarly, category 8 (excitation due to the KHF signal alone, but intrinsic activity affected spike timing) only occurred near transmission and block boundaries. This category can also be interpreted as modulation of the intrinsic activity by the KHF signal. Thus, excitation generally described KHF-evoked action potentials (category 7), potentially affected by the presence of intrinsic activity near thresholds (categories 6 and 8) where the firing rate was lower, as described below. However, given the 0.5 ms tolerance on spike time equality, the distinction between categories 7 and 8 depended upon the recording site.

We further quantified the excitation responses by computing the mean firing rate (FR_{mean}) and the firing pattern entropy. FR_{mean} (Figure 4, top) exhibited a distinct spatial banding pattern approximately parallel to the electrode with lower values near the transmission boundary and on either side of block, i.e. in fascicles neighbouring the band of block described above. More generally, the banding pattern was not exclusively spatial: FR_{mean} progressed from low to high to low, up to block, then low to high as the electrode-fibre distance was decreased, I_{KHF} was increased, or the kilohertz frequency was decreased, as exemplified by the 2 μm axons in Figure 4. This non-monotonic pattern echoes in vivo findings of higher then lower firing rates as I_{KHF} was increased [18,48,49].

Including the 100 Hz intrinsic activity only affected FR_{mean} near the transmission boundary (i.e. excitation threshold) for 1 and 2 μm axons, particularly for lower kilohertz frequencies, where FR_{mean} was increased by approximately 70 to 110 Hz, but remained low compared to other excitation cases. The effect was not observed for the 5.7 μm axons because their responses showed greater FR_{mean} overall and a much greater spatial rate of change of FR_{mean} (Figure 3); thus, their increased excitability facilitated dominance of the I_{KHF}-evoked activity over the intrinsic activity. FR_{mean} was the same for 250 and 2000 ms simulations (data not shown).

While the mean firing rate enabled quantification of the neural activity in cases of excitation, the entropy further elucidated the patterns of activity within a given spike train, where lower

entropy corresponds to more regular firing (i.e. consistent ISIs). As shown in Figure 4 (bottom), the entropy was higher near the transmission and block boundaries, typically ranging from 0.5 to 1.5 bits/spike, away from which it approached zero. The increased excitability of the 5.7 μm axons resulted in highly regular firing for most excitation cases, as reflected in the near-zero entropy values. Thus, the entropy showed many trends similar to those of FR_{mean}, including spatial banding, albeit less clearly. The entropy estimates were generally only affected by the intrinsic activity near the transmission boundary, as with FR_{mean}, although removing I_{test} resulted in instances of both higher and lower entropy in these areas.

Adjacent to the transmission and block boundaries, we observed lower FR_{mean} and higher entropy, indicating fewer action potentials with variable ISIs. Conversely, away from these threshold boundaries, the entropy was consistently near zero, indicating constant ISIs, whereas FR_{mean} varied with the electrode-fibre distance. These observations are consistent with published single unit recordings showing increasing FR_{mean} and more regular firing (i.e. low entropy) with larger KHF amplitude in the excitation regime, followed by decreasing FR_{mean} and less regular firing (i.e. higher entropy) near block threshold [49]. To clarify the relationship between FR_{mean} and entropy, we plotted these parameters in Figure 5 across all excitation cases for each fibre diameter, recalling that entropy is independent of the firing rate when the ISIs are logarithmically binned [46]. All fibre diameters exhibited a clear cluster of very low entropy with a range of high firing rates, representing the excitation cases non-adjacent to the transmission and block thresholds. The remaining data points had greater spread, albeit with clusters of low firing rate with a range of higher entropy values, reflecting the aforementioned boundary effects for the 1 and 2 μm axons. This cluster was absent in the 5.7 μm results given the larger axons' rapid spatial rate of change from transmission or block to regular high frequency firing; smaller increments in I_{KHF} would likely be needed to reveal low FR_{mean} responses with high entropy for the 5.7 μm fibres. Including the 100 Hz intrinsic activity merely shifted the lowest FR responses in the 1 μm axons up to ~100 Hz.

3.2. Electrode Design and Encapsulation Tissue

We compared the results using the EnteroMedics partial cuff [30] to a full circumneural cuff and to a point source electrode in a homogeneous isotropic infinite medium. The full cuff design shifted the pattern of conduction responses from banding (Figure 3, top) to concentric rings with approximate radial symmetry (Figure 3, middle). The full cuff resulted in higher thresholds for axons close to the partial cuff, but lower thresholds for axons far from the partial cuff, in keeping with the current-distance relationship.

The point source resulted in patterns of excitation, block, and re-excitation similar to those generated by the partial cuff electrode (Figure 3, top vs. bottom), albeit with higher spatial rate of change and many instances of re-block, i.e. block at amplitudes above those producing re-excitation. The results with 1 μm axons clearly showed a steeper threshold-distance relationship with the point source than with the partial cuff: axons with smaller electrode-fibre distances had lower thresholds with the point source than the partial cuff, while farther axons had higher thresholds. This is consistent with the comparison of the

second spatial differences of the extracellular potential ($\Delta^2 V_e(x)$) for the point source versus the partial cuff at two electrode-fibre distances (Figure 6), where $\Delta^2 V_e(x)$ is the source term driving changes in transmembrane potential [50]; at a distance of 0.45 mm, the point source produced a larger peak in $\Delta^2 V_e(x)$ than the partial cuff, whereas the peak was smaller at a distance of 3.1 mm. Indeed, $V_e(x)$ undergoes greater broadening with increased electrode-fibre distances (spatial low-pass filtering) with the point source than with the FEM.

Removing the encapsulation tissue had little impact on the KHF conduction responses and reduced the excitation and block thresholds by <1 mA. Increasing the resistivity of the encapsulation tissue (6.3 Ω–m [35]) to that of fat, as used for the extraneural medium (30 Ω–m [34]), resulted in a slightly larger potential drop between the electrode and the nerve. However, once scaled by the total current on the electrode surface as described in the Methods, the potentials were in fact higher without the encapsulation tissue due to the smaller total current, resulting in slightly lower thresholds.

3.3. Intrinsic Firing Rate

The range of firing rates observed in the vagus nerve varies depending on the type of fibre and the state of its input, including gastric stretch receptors (near quiescent [<10 Hz] when the stomach is empty, peaking at ~100 Hz, and stabilizing at tens of hertz [51,52]); gastric afferent responses to glutamate (up to 80 Hz [52]); and gastric efferents (<1 to 30 Hz with the stomach empty [53]). Thus, in addition to our default value of 100 Hz, we tested intrinsic firing rates of 20 Hz (starting at t = 25 ms) and 1 Hz (single pulse at t = 125 ms to avoid the onset response in cases of block) with the 2 μm model axon. Lower intrinsic firing rates resulted exclusively in a few cases of transmission shifting to excitation, i.e. lower excitation threshold. However, all such cases were minor modulations of the intrinsic activity. Specifically, transitions from transmission with 100 Hz to excitation with 20 Hz intrinsic activity merely reflected modulation of one or two of the five 20 Hz action potentials to doublets. Similarly, certain axons showing transmission with 20 Hz intrinsic activity were relabelled as excited when their single 1 Hz action potential became a doublet at the recording site. Thus, the frequency of intrinsic activity did not significantly affect the conduction responses produced by the KHF signals.

3.4. Mechanisms of Re-excitation

Our simulations revealed a novel phenomenon, where we observed excitation, i.e. KHF-evoked activity, at stimulation amplitudes above those producing block, a condition we termed "re-excitation". We found that action potentials initiated at different locations along the axon for re-excitation than for initial excitation with amplitudes below the block threshold. To understand the phenomenon of re-excitation, recall that the response of the transmembrane potential along the axon ($V_m(x)$) to extracellular stimulation is triphasic (Figure 7): a cathodic (negative) current causes a depolarized central lobe ("true cathode") and hyperpolarized side lobes ("virtual anodes"), whereas the response is inverted in response to an anodic (positive) current. This well-established phenomenon is responsible for the bands of block observed. In select cases, we made videos of $V_m(x)$ and found that in excitation, action potentials were initiated at the true cathode, i.e. under the centre of the cuff

electrode during the cathodic phase of the KHF signal. Conversely, in re-excitation, action potentials were initiated at the virtual cathodes during the anodic phase of the KHF signal.

We investigated why re-excitation has not been previously reported. We ran simulations with 10 and 16 μm MRG model axons [39] at 5, 10, and 20 kHz to compare with previous computational studies [18]. Using a point source 1 mm from each fibre, we found that we could not produce re-excitation in these larger diameter model axons, even with the amplitude resolution refined to 0.01 mA. With increasing amplitude, the smaller axons progressed from excitation (action potentials initiated at the true cathode), to block (h near zero under the electrode's centre causing Na^+ channel inactivation [9]), to re-excitation (action potentials initiated at the virtual cathodes), as illustrated in Supplemental Videos 1–3[1]. Conversely, the larger axons simply progressed from excitation to block, although the block location (i.e. where h approached zero) shifted from under the electrode's centre to off-centre (Supplemental Videos 4–5[1]).

The results with the point source electrode revealed an additional level of complexity (Figure 3, bottom). The 5.7 μm axons with the smallest electrode-fibre distances were in a state of re-block due to action potential arrest in areas of low h at the virtual anodes. As the amplitude was increased for a given frequency, a second band of block appeared at intermediate electrode-fibre distances. However, the band of excitation at lower amplitudes actually included both excitation responses (for farther axons) and re-excitation responses (for closer axons), with instances of block in between that were not revealed with the chosen electrode-fibre distances. This condensed spatial pattern of the different neural responses – as compared to the clear bands obtained with the partial cuff – is consistent with the greater spatial rate of change of peak potentials and second differences with the point source than with the FEM.

4. Discussion

There is growing interest in peripheral nerve stimulation to treat a variety of diseases, as well as in KHF neuromodulation to enable block of neural signals. We developed a computational model to investigate the effects of KHF electrical signals delivered via a cuff electrode to a compound peripheral nerve across a range of amplitudes, frequencies, fibre diameters, and electrode designs.

4.1. Conduction Responses Mirror Conventional Stimulation Trends and Reveal Asynchronous Activity

The effects of signal amplitude, electrode-fibre distance, and axon diameter on the responses to KHF signals were analogous to those of conventional stimulation at 10's to 100's of Hz: less transmission for larger KHF amplitudes, closer electrode-fibre distances, and larger

---

[1]Each video shows the transmembrane potential (V_m) and the four gating parameters of the MRG model [39] (m and h for the fast sodium current, p for the persistent sodium current, and s for the potassium current) as functions of the distance along the axon. The horizontal dashed lines indicate the rest values. The videos include the first 32 ms of each simulation, but we observed similar behaviour out to 250 ms. The vertical axis limits are consistent across the videos. Consequently, some data are out of bounds, indicated in parentheses. Video 1: 2 μm axon, 4 mA, showing excitation. Video 2: 2 μm axon, 7 mA, showing block. Video 3: 2 μm axon, 12 mA, showing re-excitation. Video 4: 10 μm axon, 1 mA, showing block (−110 to 67 mV). Video 5: 10 μm axon, 4 mA, showing block (−260 to 141 mV).

fibre diameters, consistent with previously reported trends for conduction block [18]. In addition, lower kilohertz frequencies also had lower excitation and block thresholds, analogous to the strength-duration phenomenon for conventional cathodic pulses [47]. More specifically, the phase duration of the KHF waveform increases at lower frequencies for full duty cycle rectangular waveforms, as used herein, as well as for sinusoidal waveforms. The non-linear response of the fast sodium channel results in a greater change in transmembrane potential during depolarization than hyperpolarization. Thus, during the longer cathodic phase at lower KHF, there is a greater net depolarization under the electrode than at higher frequencies, resulting in smaller thresholds for both excitation and block. The trend of increased block threshold with frequency was previously demonstrated in vivo for sinusoidal stimulation [54]. Lastly, we observed that amplitude had a lesser effect at higher frequencies; in other words, the slope of threshold as a function of electrode-fibre distance was steeper at higher KHF.

Our simulations revealed a new phenomenon termed re-excitation, describing continual KHF-evoked action potentials at closer electrode-fibre distances, larger amplitudes, and lower frequencies than required to sustain block. Re-excitation occurred as a result of action potential initiation at virtual cathodes during the anodic phase of the KHF waveform, as opposed to initiation at the true cathode during the cathodic phase. Thus, although the nodes of Ranvier under the electrode's centre remained in a blocked state, KHF-evoked action potentials initiated laterally and propagated in both directions. Whether re-excitation can occur in vivo at non-damaging stimulation amplitudes is unclear. We found that re-excitation could not be produced in larger diameter model axons given that their block location (i.e. h approaching zero causing Na+ inactivation) shifted symmetrically laterally at larger amplitudes.

We quantified the excitation responses by computing the mean firing rate and entropy. Although our method for computing entropy was independent of the firing rate [46], we observed coincident lower firing rates and higher entropy values near the block and transmission boundaries. Indeed, at electrode-fibre distances resulting in excitation or re-excitation away from these boundaries, the KHF-evoked activity was highly regular (i.e. low entropy) with firing rates dependent on the electrode-fibre distance. This is consistent with previous single unit recordings in cat dorsal roots showing an increase in firing rate and spike regularity followed by a decrease as the KHF amplitude approached block threshold [49]. Thus, although our simulations revealed a high occurrence of excitation and re-excitation (Figure 3), these KHF-evoked spike trains spanned a wide range of patterns and firing rates (Figure 4 and Figure 5), indicating a lack of synchronous activity. Therefore, the compound nerve exhibited highly asynchronous activity, suggesting that recordings of compound action potentials or downstream muscle force measurements may not be reliable quantitative measures of neural activity for in vivo studies or as biomarkers in closed-loop clinical devices.

In cases of excitation, the mean firing rates were as high as 700 Hz under some conditions (Figure 4 and Figure 5). Bowman and McNeal (1986) observed similar firing rates in peripheral motor axons in response to 4 kHz stimulation [48] and Crosby et al. (2017) observed firing rates of dorsal column axons in excess of 200 Hz in response to KHF spinal

cord stimulation [55]. However, it remains unclear whether small diameter autonomic nerve fibers can sustain such high firing rates.

The point source in a homogeneous isotropic medium yielded results similar to those with the FEM in terms of approximate excitation and block thresholds. However, the point source threshold-distance relationship had a steeper slope, and we observed higher order responses, such as re-block. The FEM simulations did not show any instances of re-block, despite amplitudes well above re-excitation threshold, suggesting that such responses may not occur in vivo.

Removing the encapsulation tissue from the partial cuff had little effect, but transitioning to a fully circumferential cuff shifted the conduction response from banding patterns to approximate radial symmetry, although the width of the bands/rings of block were not wider. Changing the intrinsic firing rate from 1 to 100 Hz did not affect the conduction responses.

4.2. Clinical Implications: Block of Abdominal Vagus is Unlikely

EnteroMedics developed and continues to market vBloc® therapy for treatment of obesity based on the premise that the 5 kHz electrical signals delivered to the anterior and posterior vagus nerves block neural conduction, thereby producing weight loss via delayed gastric emptying from suppressed contractions, reduced gastric accommodation, or suppressed ghrelin release (appetite-stimulating hormone [56]) [13,14,31]. However, the results herein indicate that the predominant effect of the 5 kHz signals is not conduction block. Rather, at the typical clinical settings of 5 kHz and 6 mA, the small myelinated model fibres generally exhibited KHF-evoked activity (excitation and re-excitation) with a range of firing rates (higher FR_{mean} for larger fibres) and patterns (lower entropy for larger fibres). Although there are a large number of unmyelinated fibres in the abdominal vagi, their thresholds are expected to be significantly higher than the clinical amplitudes [57,58]. Thus, these findings may explain the failure of the two vBloc® clinical trials to achieve their primary efficacy end points. Conversely, the results may suggest alternative mechanisms of action, such as evoked satiety signals transmitted to the brainstem via afferent excitation, mimicking signals that are normally induced via gastric stretch receptors and receptors for hormones released in response to nutrients following feeding [56].

4.3. Limitations of Computational Model

Several simplifying assumptions were made during model development and simulation. All axons were aligned with a node of Ranvier under the electrode centre, rather than jittering their longitudinal placement within one internodal distance. Randomizing their alignment was not expected to affect the results given the large electrode-fibre distances (0.45 to 3.06 mm to the electrode centre) [18,59,60] and the broad potential profile resulting from the cuff electrode (Figure 6) as compared to the internodal lengths (0.1, 0.2, and 0.5 mm for the 1, 2, and 5.7 µm model axons, respectively).

We assumed quasi-static conditions and ignored capacitive, inductive, and wave propagation effects. We also neglected the dispersive properties of the tissues, meaning we did not include frequency-dependent conductivity. Previous analysis showed that the inductive and

wave propagation effects can be neglected when modeling neural stimulation [61]. This study compared potentials and stimulation effects from a 100 μs cathodic pulse with the quasi-static solution versus the full Helmholtz equation with dispersion for grey matter. They found that the accuracy of the conductivity values is more important than the error introduced via the quasi-static and non-dispersive assumptions. Since the power spectra of the 100 μs pulses and the KHF waveforms used herein span comparable ranges, we may also assume that errors introduced by the quasi-static assumption are within an acceptable range. However, if we were to test higher kilohertz frequencies (100 kHz and above) that have been examined in other publications (e.g. [62,63]), then the quasi-static assumption may no longer be appropriate. Furthermore, there is a lack of available data on the permittivities and frequency-dependent conductivities of the tissues in compound peripheral nerves [64]. We did not include a representation of the electrode tissue interface impedance [65,66] because this will not affect the spatiotemporal distribution of potentials generated by current-controlled electrical signals [65,66].

The MRG model of myelinated mammalian axons has been extensively validated against published experimental data, including responses to conventional stimulation (action potential shape, afterpotentials, recovery cycle, conduction speed, strength-duration curve [39]), as well as KHF phenomena (block threshold trends with frequency [17,18,54,67,68], effects of persistent sodium conductance [17], and onset response [18,21,48,54,67,68]). However, the models of 1 and 2 μm axons have not been validated. Further, future models may be improved to include frequency-dependent axonal membrane capacitance [69].

At the time of model development, we based the fascicle sizes on published histology images [29], although the cross-sections are a few vertebral levels higher than the subdiaphragmatic abdominal vagus nerve trunks. Subsequent examination of cadaveric human abdominal vagus nerve samples revealed fascicle diameters approximately one third of those used in this publication. Initial simulations show a moderate shift towards lower thresholds for excitation (0 to 6 mA shift) and block (1 to 2 mA shift) with smaller fascicles, as expected from previous investigations [70]. However, the trends and phenomena described herein remain valid.

We briefly investigated the impact of certain FEM parameter values as described throughout this report (model height, medium radius, fascicle radii, encapsulation tissue, and endoneurial resistivity), but we did not include sensitivity analyses to other parameters, including fascicle number, epineurial resistivity, and perineurial specific resistance. The inclusion of all fascicles is known to be important for accurate estimation of stimulation thresholds [70]; while we did not investigate the effect of fascicle number or density herein, the results in Grinberg et al. (2008) [70] suggest that our thresholds could be affected by <5% given the physiologically relevant range of fascicle sizes and densities. A wide range of epineurial conductivities were used in previous models (1 to 125 Ω-m [70–76]), but most used 12 Ω-m as originally chosen by Choi et al. 2001 [71], equal to the radial endoneurial resistivity because of the "similarity between the connective tissue". However, the radial endoneurial resistivity is a bulk value accounting for both the axons and the connective tissue. Thus, our epineurial resistivity (6.3 Ω-m) instead corresponds to the resistivity of encapsulation tissue, since the epineurium and encapsulation are both indeed similar

collagenous connective tissues. Lastly, the perineurium constitutes a highly resistive sheath of connective tissue surrounding each fascicle, which is important for accurate threshold estimates [70]. The perineurium has been assigned various estimates of resistivity and thickness in published models (e.g., [58,70,71,73–77]). Using a simplified model with a single fascicle, we compared cathodic thresholds for 2 μm axons using the specific resistance of 0.05 Ω-m^2 as used herein versus a resistivity of 500 Ω-m and a perineurial thickness of 3% of the fascicle diameter [70] which we used to compute the contact resistance. Comparing the two models, we found 24 and 36% decreases in threshold for axons within a small fascicle (70 μm radius) and a large fascicle (225 μm radius), respectively.

5. Conclusions

Our modeling results suggest that KHF electrical signals delivered to the human abdominal vagus nerves via cuff electrodes do not generate conduction block uniformly across the nerve. Rather, continual asynchronous KHF-evoked activity was the predominant response when the signal was suprathreshold, with the effects of amplitude, axon diameter, and electrode-fibre distance paralleling those for conventional stimulation. We observed a new phenomenon termed "re-excitation" where KHF-evoked activity occurred at amplitudes above block threshold, thus producing banding patterns of conduction responses with a partial cuff electrode and concentric rings with a full cuff. We classified the neural responses and associated mechanisms of action of the effects of KHF signals through our novel FEM and small model axons, thus providing important understanding and knowledge for further development of peripheral nerve stimulation therapies.

Supplementary Material

Refer to Web version on PubMed Central for supplementary material.

Acknowledgments

References

1. Birmingham K, Gradinaru V, Anikeeva P, Grill WM, Pikov V, McLaughlin B, Pasricha P, Weber D, Ludwig K, Famm K. Bioelectronic medicines: a research roadmap. Nat Rev Drug Discov. 2014; 13:399–400. [PubMed: 24875080]

2. Famm K, Litt B, Tracey KJ, Boyden ES, Slaoui M. Drug discovery: a jump-start for electroceuticals. Nature. 2013; 496:159–61. [PubMed: 23579662]

3. Waltz E. A spark at the periphery. Nat Biotechnol. 2016; 34:904–8. [PubMed: 27606451]

4. McGee MJ, Grill WM. Temporal pattern of stimulation modulates reflex bladder activation by pudendal nerve stimulation. Neurourol Urodynam. 2015; 35:882–7.

5. Ikramuddin S, Blackstone RP, Brancatisano A, Toouli J, Shah SN, Wolfe BM, Fujioka K, Maher JW, Swain J, Que FG, Morton JM, Leslie DB, Brancatisano R, Kow L, O'Rourke RW, Deveney C, Takata M, Miller CJ, Knudson MB, Tweden KS, Shikora SA, Sarr MG, Billington CJ. Effect of

reversible intermittent intra-abdominal vagal nerve blockade on morbid obesity: the ReCharge randomized clinical trial. JAMA. 2014; 312:915–22. [PubMed: 25182100]

6. Koopman FA, Chavan SS, Miljko S, Grazio S, Sokolovic S, Schuurman PR, Mehta AD, Levine YA, Faltys M, Zitnik R, Tracey KJ, Tak PP. Vagus nerve stimulation inhibits cytokine production and attenuates disease severity in rheumatoid arthritis. P Natl Acad Sci USA. 2016; 113:8284–9.

7. Gold MR, van Veldhuisen DJ, Mann DL. Vagal nerve stimulation for heart failure: new pieces to the puzzle?: Editorial. Eur J Heart Fail. 2015; 17:125–7. [PubMed: 25678096]

8. Shikora S, Toouli J, Herrera MF, Kulseng B, Zulewski H, Brancatisano R, Kow L, Pantoja JP, Johnsen G, Brancatisano A, Tweden KS, Knudson MB, Billington CJ. Vagal blocking improves glycemic control and elevated blood pressure in obese subjects with type 2 diabetes mellitus. J Obes. 2013; 2013:245683. [PubMed: 23984050]

9. Kilgore KL, Bhadra N. Reversible nerve conduction block using kilohertz frequency alternating current: reversible KHFAC nerve block. Neuromodulation. 2014; 17:242–55. [PubMed: 23924075]

10. Al-Kaisy A, Van Buyten J-P, Smet I, Palmisani S, Pang D, Smith T. Sustained effectiveness of 10 kHz high-frequency spinal cord stimulation for patients with chroniclow back pain: 24-month results of a prospective multicenter study. Pain Med. 2014; 15:347–54. [PubMed: 24308759]

11. Soin A, Syed Shah N, Fang Z-P. High-frequency electrical nerve block for postamputation pain: a pilot study. Neuromodulation. 2015; 18:197–206. [PubMed: 25655583]

12. Shikora SA, Wolfe BM, Apovian CM, Anvari M, Sarwer DB, Gibbons RD, Ikramuddin S, Miller CJ, Knudson MB, Tweden KS, Sarr MG, Billington CJ. Sustained weight loss with vagal nerve blockade but not with sham: 18-month results of the ReCharge trial. J Obes. 2015; 2015:1–8.

13. Ikramuddin S, Blackstone RP, Brancatisano A, Toouli J, Shah SN, Wolfe BM, Fujioka K, Maher JW, Swain J, Que FG, Morton JM, Leslie DB, Brancatisano R, Kow L, O'Rourke RW, Deveney C, Takata M, Miller CJ, Knudson MB, Tweden KS, Shikora SA, Sarr MG, Billington CJ. Effect of reversible intermittent intra-abdominal vagal nerve blockade on morbid obesity: the ReCharge randomized clinical trial -Supplement 1, trial protocol. JAMA. 2014; 312:915–22. [PubMed: 25182100]

14. Sarr MG, Billington CJ, Brancatisano R, Brancatisano A, Toouli J, Kow L, Nguyen NT, Blackstone R, Maher JW, Shikora S, Reeds DN, Eagon JC, Wolfe BM, O'Rourke RW, Fujioka K, Takata M, Swain JM, Morton JM, Ikramuddin S, Schweitzer M, Chand B, Rosenthal R. The EMPOWER study: randomized prospective double-blind multicenter trial of vagal blockade to induce weight loss in morbid obesity. Obes Surg. 2012; 22:1771–82. [PubMed: 22956251]

15. McNeal DR. Analysis of a model for excitation of myelinated nerve. IEEE T Biomed Eng. 1976; BME-23:329–37.

16. Joucla S, Yvert B. Modeling extracellular electrical neural stimulation: from basic understanding to MEA-based applications. J Physiology-Paris. 2012; 106:146–58.

17. Ackermann DM, Bhadra N, Gerges M, Thomas PJ. Dynamics and sensitivity analysis of high-frequency conduction block. J Neural Eng. 2011; 8:065007. [PubMed: 22056338]

18. Bhadra N, Lahowetz EA, Foldes ST, Kilgore KL. Simulation of high-frequency sinusoidal electrical block of mammalian myelinated axons. J Comput Neurosci. 2007; 22:313–26. [PubMed: 17200886]

19. Joseph L, Haeffele BD, Butera RJ. Conduction block induced by high frequency AC stimulation in unmyelinated nerves. Conf Proc IEEE Eng Med Biol Soc. 2007; 2007:1719–22. [PubMed: 18002307]

20. Kilgore KL, Bhadra N. Nerve conduction block utilising high-frequency alternating current. Med Biol Eng Comput. 2004; 42:394–406. [PubMed: 15191086]

21. Miles JD, Kilgore KL, Bhadra N, Lahowetz EA. Effects of ramped amplitude waveforms on the onset response of high-frequency mammalian nerve block. J Neural Eng. 2007; 4:390–8. [PubMed: 18057506]

22. Tai C, Guo D, Wang J, Roppolo JR, de Groat WC. Mechanism of conduction block in amphibian myelinated axon induced by biphasic electrical current at ultra-high frequency. J Comput Neurosci. 2011; 31:615–23. [PubMed: 21523417]

23. Tai C, deGroat WC, Roppolo JR. Simulation of nerve block by high-frequency sinusoidal electrical current based on the Hodgkin-Huxley model. IEEE Trans Neural Syst Rehabil Eng. 2005; 13:415–22. [PubMed: 16200764]

24. Pelot NA, Behrend CE, Grill WM. Modeling the response of small myelinated and unmyelinated axons to kilohertz frequency signals 7th International IEEE/EMBS Conference on Neural Engineering (IEEE). 2015:406–9.

25. Ranck JB Jr, Bement SL. The specific impedance of the dorsal columns of cat: an anisotropic medium. Exp Neurol. 1965; 11:451–63. [PubMed: 14278100]

26. Mei N, Condamin M, Boyer A. The composition of the vagus nerve of the cat. Cell Tissue Res. 1980; 209:423–31. [PubMed: 7407841]

27. Prechtl JC, Powley TL. The fiber composition of the abdominal vagus of the rat. Anat Embryol. 1990; 181:101–15. [PubMed: 2327594]

28. Tailai Z, Junsheng T, Zuxun Z, Baokang Z, Yunping M. Vagus nerve anatomy at the lower esophagus and stomach. Chinese Med J-Peking. 1980; 93:629–36.

29. Kawagishi K, Fukushima N, Yokouchi K, Sumitomo N, Kakegawa A, Moriizumi T. Tyrosine hydroxylase-immunoreactive fibers in the human vagus nerve. J Clin Neurosci. 2008; 15:1023–6. [PubMed: 18617399]

30. Foster AJ, Erickson BJ, Bierk MD. Custom sized neural electrodes. 2010

31. Camilleri M, Toouli J, Herrera MF, Kulseng B, Kow L, Pantoja JP, Marvik R, Johnsen G, Billington CJ, Moody FG, Knudson MB, Tweden KS, Vollmer M, Wilson RR, Anvari M. Intra-abdominal vagal blocking (VBLOC therapy): clinical results with a new implantable medical device. Surgery. 2008; 143:723–31. [PubMed: 18549888]

32. Haberler C, Alesch F, Mazal PR, Pilz P, Jellinger K, Pinter MM, Hainfellner JA, Budka H. No tissue damage by chronic deep brain stimulation in Parkinson's disease. Ann Neurol. 2000; 48:372–6. [PubMed: 10976644]

33. Moss J, Ryder T, Aziz TZ, Graeber MB, Bain PG. Electron microscopy of tissue adherent to explanted electrodes in dystonia and Parkinson's disease. Brain. 2004; 127:2755–63. [PubMed: 15329356]

34. Geddes LA, Baker LE. The specific resistance of biological material - A compendium of data for the biomedical engineer and physiologist. Med Biol Eng. 1967; 5:271–93. [PubMed: 6068939]

35. Grill WM, Mortimer JT. Electrical properties of implant encapsulation tissue. Ann Biomed Eng. 1994; 22:23–33. [PubMed: 8060024]

36. Stolinski C. Structure and composition of the outer connective tissue sheaths of peripheral nerve. J Anat. 1995; 186(Pt 1):123–30. [PubMed: 7649808]

37. Weerasuriya A, Spangler RA, Rapoport SI, Taylor RE. AC impedance of the perineurium of the frog sciatic nerve. Biophys J. 1984; 46:167–74. [PubMed: 6332648]

38. Carnevale, NT., Hines, ML. The NEURON Book. Cambridge UK: Cambridge University Press; 2006.

39. McIntyre CC, Richardson AG, Grill WM. Modeling the excitability of mammalian nerve fibers: influence of afterpotentials on the recovery cycle. J Neurophysiol. 2002; 87:995–1006. [PubMed: 11826063]

40. McIntyre CC, Grill WM, Sherman DL, Thakor NV. Cellular effects of deep brain stimulation: model-based analysis of activation and inhibition. J Neurophysiol. 2004; 91:1457–69. [PubMed: 14668299]

41. Guo YP, McLeod JG, Baverstock J. Pathological changes in the vagus nerve in diabetes and chronic alcoholism. J Neurol Neurosurg Psychiatr. 1987; 50:1449–53. [PubMed: 3694205]

42. Boyd IA, Kalu KU. Scaling factor relating conduction velocity and diameter for myelinated afferent nerve fibres in the cat hind limb. J Physiol-London. 1979; 289:277–97. [PubMed: 458657]

43. Duclaux R, Mei N, Ranieri F. Conduction velocity along the afferent vagal dendrites: a new type of fibre. J Physiol-London. 1976; 260:487–95. [PubMed: 978547]

44. Zotova EG, Arezzo JC. Noninvasive evaluation of nerve conduction in small diameter fibers in the rat. Physiology Journal. 20132013:1–11.

45. Sivagnanam S, Majumdar A, Yoshimoto K, Astakhov V, Bandrowski A, Martone ME, Carnevale NT. Introducing the Neuroscience Gateway. IWSG - CEUR Workshop Proceedings. 2013; 993

46. Dorval AD. Probability distributions of the logarithm of inter-spike intervals yield accurate entropy estimates from small datasets. J Neurosci Meth. 2008; 173:129–39.

47. Lozano AM, Hallett M. Brain Stimulation: Handbook of Clinical Neurology (Series editors: Aminoff, Boller, Swaab) (Newnes). 2013

48. Bowman BR, McNeal DR. Response of single alpha motoneurons to high-frequency pulse trains. Firing behavior and conduction block phenomenon. Appl Neurophysiol. 1986; 49:121–38. [PubMed: 3827239]

49. Woo MY, Campbell B. Asynchronous firing and block of peripheral nerve conduction by 20 KC alternating current. Bull Los Angel Neuro Soc. 1964; 29:87–94. [PubMed: 14169956]

50. Rattay F. Analysis of models for external stimulation of axons. IEEE Trans Biomed Eng. 1986; 33:974–7. [PubMed: 3770787]

51. Paintal AS. Vagal afferent fibres. Erg Physiol Biol Ch. 1963; 52:74–156.

52. Uneyama H, Niijima A, San Gabriel A, Torii K. Luminal amino acid sensing in the rat gastric mucosa. Am J Physiol-Gastr L. 2006; 291:G1163–70.

53. Davison JS, Grundy D. Modulation of single vagal efferent fibre discharge by gastrointestinal afferents in the rat. J Physiol-London. 1978; 284:69–82. [PubMed: 731576]

54. Bhadra N, Kilgore KL. High-frequency electrical conduction block of mammalian peripheral motor nerve. Muscle Nerve. 2005; 32:782–90. [PubMed: 16124008]

55. Crosby ND, Janik JJ, Grill WM. Modulation of activity and conduction in single dorsal column axons by kilohertz-frequency spinal cord stimulation. J Neurophysiol. 2017; 117:136–47. [PubMed: 27760823]

56. Berthoud H-R. The vagus nerve food intake and obesity. Regul Peptides. 2008; 149:15–25.

57. Li CL, Bak A. Excitability characteristics of the A- and C-fibers in a peripheral nerve. Experimental Neurology. 1976; 50:67–79. [PubMed: 1248547]

58. Yoo PB, Lubock NB, Hincapie JG, Ruble SB, Hamann JJ, Grill WM. High-resolution measurement of electrically-evoked vagus nerve activity in the anesthetized dog. Journal of Neural Engineering. 2013; 10:026003. [PubMed: 23370017]

59. Rattay F. Ways to approximate current-distance relations for electrically stimulated fibers. J Theor Biol. 1987; 125:339–49. [PubMed: 3657215]

60. McIntyre CC, Grill WM. Excitation of central nervous system neurons by nonuniform electric fields. Biophys J. 1999; 76:878–88. [PubMed: 9929489]

61. Bossetti CA, Birdno MJ, Grill WM. Analysis of the quasi-static approximation for calculating potentials generated by neural stimulation. J Neural Eng. 2008; 5:44–53. [PubMed: 18310810]

62. Patel Y, Butera RJ. Differential fiber-specific block of nerve conduction in mammalian peripheral nerves using kilohertz electrical stimulation. J Neurophysiol. 2015; 113:3923–9. [PubMed: 25878155]

63. Zhao S, Yang G, Wang J, Roppolo JR, de Groat WC, Tai C. Conduction block in myelinated axons induced by high-frequency (kHz) non-symmetric biphasic stimulation. Frontiers in Computational Neuroscience. 2015; 9:86. [PubMed: 26217217]

64. Gabriel S, Lau RW, Gabriel C. The dielectric properties of biological tissues: III. Parametric models for the dielectric spectrum of tissues. Phys Med Biol. 1996; 41:2271–93. [PubMed: 8938026]

65. Cantrell DR, Inayat S, Taflove A, Ruoff RS, Troy JB. Incorporation of the electrode-electrolyte interface into finite-element models of metal microelectrodes. J Neural Eng. 2008; 5:54–67. [PubMed: 18310811]

66. Howell B, Naik S, Grill WM. Influences of interpolation error electrode geometry and the electrode-tissue interface on models of electric fields produced by deep brain stimulation. IEEE T Biomed Eng. 2014; 61:297–307.

67. Kilgore KL, Bhadra N. High frequency mammalian nerve conduction block: simulations and experiments. Conf Proc IEEE Eng Med Biol Soc. 2006; 1:4971–4. [PubMed: 17946274]

68. Bhadra N, Bhadra N, Kilgore K, Gustafson KJ. High frequency electrical conduction block of the pudendal nerve. J Neural Eng. 2006; 3:180–7. [PubMed: 16705274]

69. Howell B, Medina LE, Grill WM. Effects of frequency-dependent membrane capacitance on neural excitability. J Neural Eng. 2015; 12:056015. [PubMed: 26348707]

70. Grinberg Y, Schiefer MA, Tyler DJ, Gustafson KJ. Fascicular perineurium thickness size and position affect model predictions of neural excitation. IEEE T Neur Sys Reh. 2008; 16:572–81.

71. Choi AQ, Cavanaugh JK, Durand DM. Selectivity of multiple-contact nerve cuff electrodes: a simulation analysis. IEEE Trans Biomed Eng. 2001; 48:165–72. [PubMed: 11296872]

72. Schiefer MA, Triolo RJ, Tyler DJ. A model of selective activation of the femoral nerve with a flat interface nerve electrode for a lower extremity neuroprosthesis. IEEE Trans Neural Syst Rehabil Eng. 2008; 16:195–204. [PubMed: 18403289]

73. Kent AR, Grill WM. Model-based analysis and design of nerve cuff electrodes for restoring bladder function by selective stimulation of the pudendal nerve. Journal of Neural Engineering. 2013; 10:036010. [PubMed: 23594706]

74. Goodall EV, Kosterman LM, Holsheimer J, Struijk JJ. Modeling study of activation and propagation delays during stimulation of peripheral nerve fibers with a tripolar cuff electrode. IEEE Transactions on Rehabilitation Engineering. 1995; 3:272–82.

75. Deurloo KEI, Holsheimer J, Bergveld P. Fascicular selectivity in transverse stimulation with a nerve cuff electrode: a theoretical approach. Neuromodulation. 2003; 6:258–69. [PubMed: 22151073]

76. Perez-Orive J, Durand DM. Modeling study of peripheral nerve recording selectivity. IEEE Trans Rehabil Eng. 2000; 8:320–9. [PubMed: 11001512]

77. Koole P, Holsheimer J, Struijk JJ, Verloop AJ. Recruitment characteristics of nerve fascicles stimulated by a multigroove electrode. IEEE Trans Rehabil Eng. 1997; 5:40–50. [PubMed: 9086384]
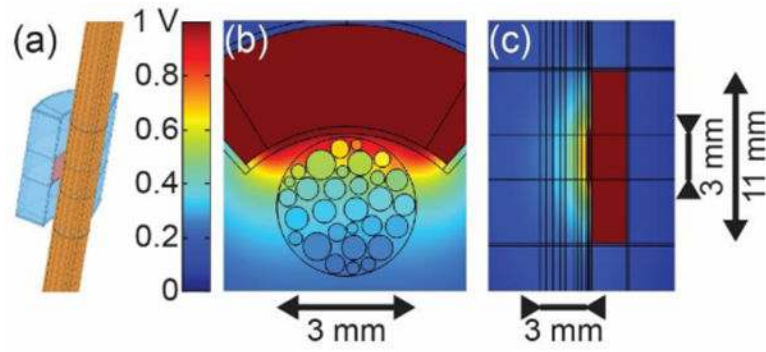
Figure 1.
(a) 3D FEM of compound nerve with cuff electrode. (b) Transverse cross-section showing the cuff electrode around the nerve containing fascicles. (c) Longitudinal cross-section showing vertical extent of cuff electrode.

Initial & final categories		Spike times $I_{test} \neq 0$	Spike times $I_{test} = 0$	Example $I_{test} \neq 0$ & $I_{test} = 0$
1) Clean transmission	Transmission	Same as $I_{KHF} = 0$	Zero spikes	
2) Transmission with onset response when $I_{test} \neq 0$, i.e. transient burst due to combination of KHF and intrinsic activity		Same as $I_{KHF} = 0$ for t > 100 ms	Zero spikes	
3) Transmission after KHF-evoked onset response		Same as $I_{KHF} = 0$ for t > 100 ms	Zero spikes for t > 100 ms	
4) Block after onset response	Block	Same; zero spikes for t > 100 ms		
5) Excitation due to combination of I_{test} and I_{KHF}	Excitation	No constraint	Zero spikes	Not observed
6) Excitation due to combination of I_{test} and I_{KHF} after KHF-evoked onset response		No constraint	Zero spikes for t > 100 ms	
7) Excitation due to I_{KHF} alone, unaffected by I_{test}		Same		
8) Excitation due to I_{KHF} alone, affected by I_{test}		Remaining cases		

Figure 2.
Data analysis algorithm. I_{test}: Intracellular test pulse near proximal end of model axon to generate intrinsic activity. I_{KHF}: Current applied at cuff electrode surface; we applied the resulting potentials at the axon's location to the model fibers extracellularly at given kilohertz frequency.
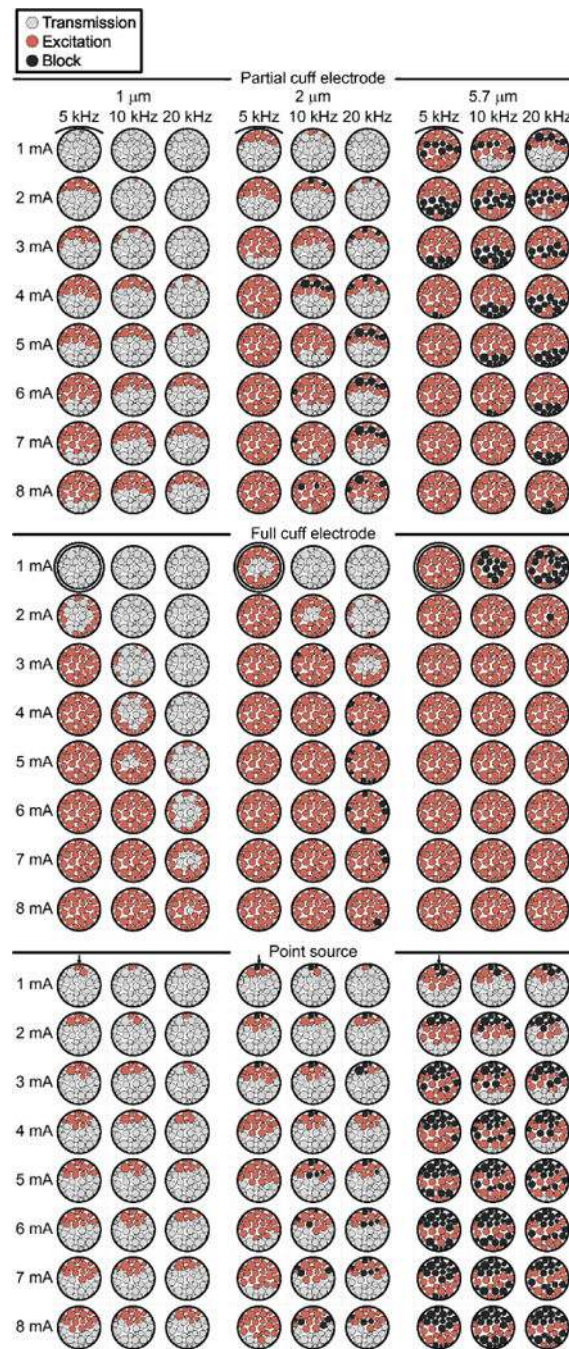
Figure 3.
Conduction responses across different myelinated axon diametersand different frequencies and amplitudes of the KHF signal. Top section: FEM with partial cuff electrode. Middle section: FEM with full circumneural cuff electrode. Bottom section: Point source in homogeneous isotropic infinite medium with electrode-fibre distances from FEM; drawn with FEM to allow visual comparison. Each fascicle is coloured uniformly since the axon position within a given fascicle did not affect the response.
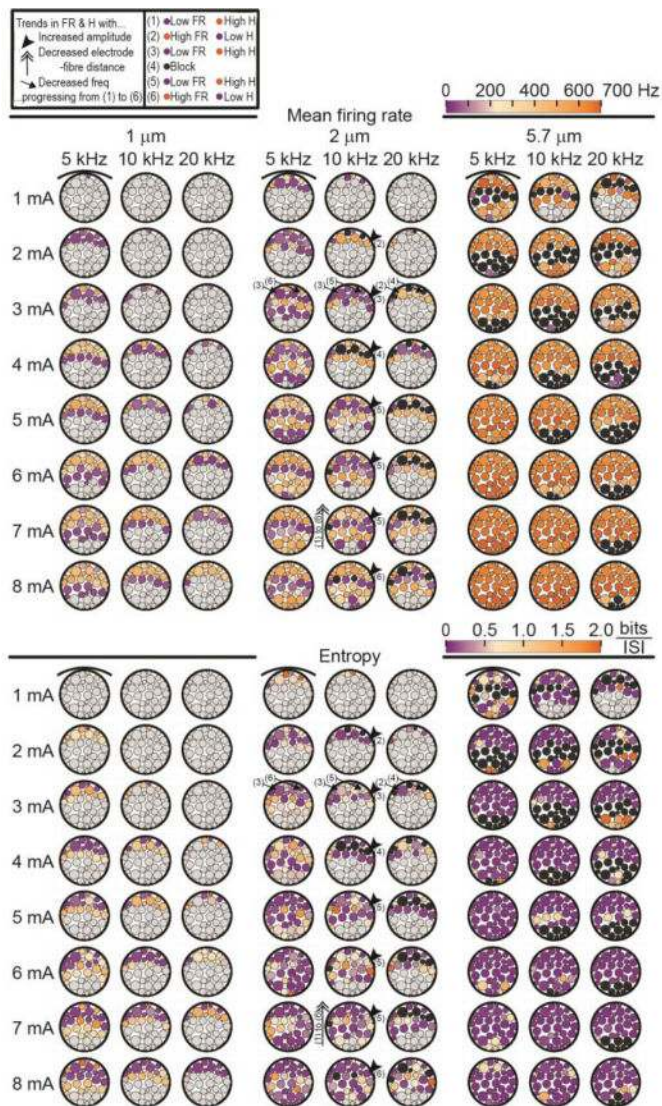
Figure 4.
Mean firing rates (top section) and entropy (bottom section) without intrinsic activity. Both output measures use the same colour bar to illustrate that lower mean firing rate (purpletop section) is generally associated with higher entropy (orangebottom section)and vice versa (see also Figure 5). The upper-left legend defines the arrows and numerical labels illustrating the trends in mean firing rate (FR) and entropy (H) from (1) to (6) as the KHF stimulation amplitude is increasedthe electrode-fibre distance is decreasedor the frequency is decreased. The arrows on the entropy plots are taken from identification of the banding patterns in the mean firing rate data to show that a similar trend exists. Black fascicles indicate block and light grey fascicles indicate transmission.
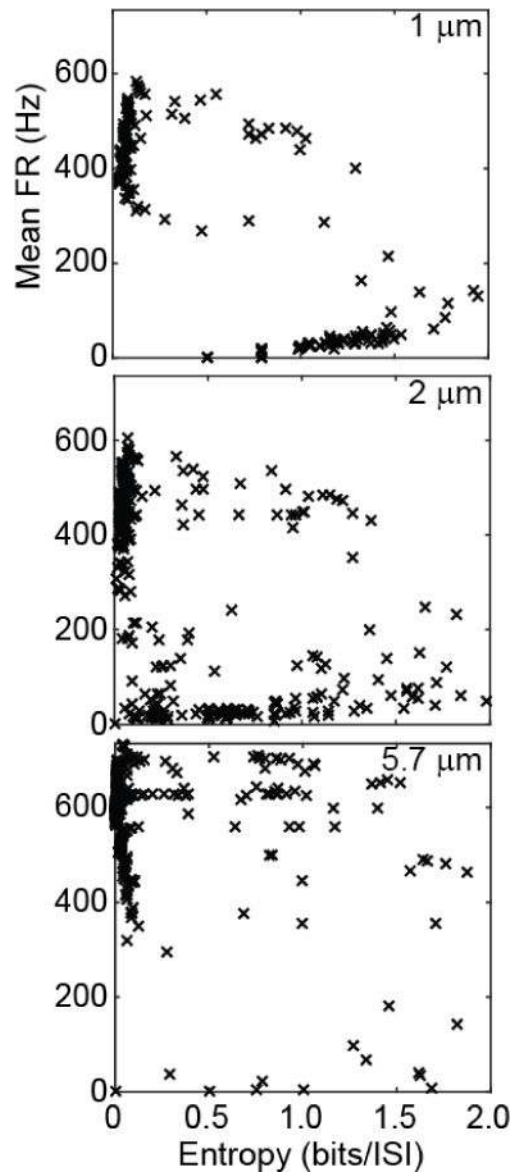
Figure 5.
Mean firing rate vs entropy for all excitation cases across the three kilohertz frequencies and eight I_{KHF} amplitudes for each fibre diameter (columns) without intrinsic activity.
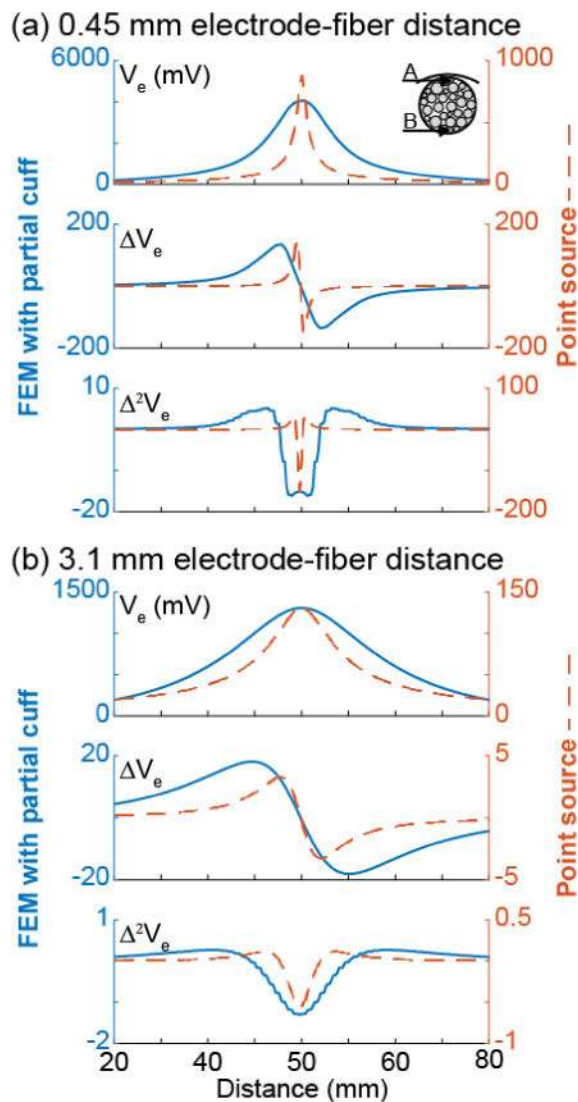
Figure 6.
Potentials and their first and second spatial differences for a 2 μm axon at two electrode-fibre distances ((a) 0.45 mm(b) 3.1 mm) from the partial cuff FEM (left axessolid lines) and from the point source (right axesdashed lines). The electrode-fibre distance was calculated from the centre of the partial cuff electrode. The second differences of the potentials for the 1 and 5.7 μm axons had the same trends. Note the different y axes.
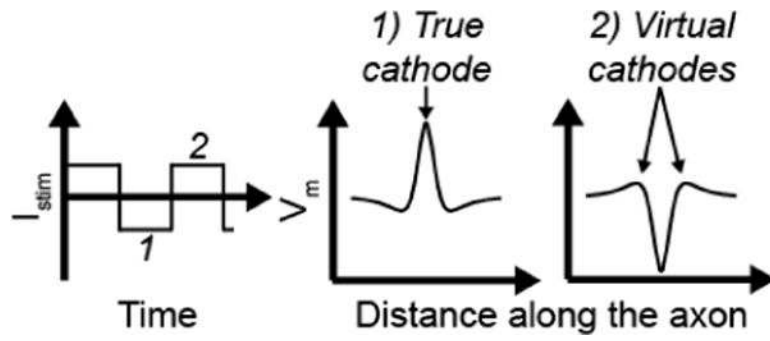
Figure 7.
Diagram of the spatially triphasic transmembrane response to extracellular cathodic (1) and anodic (2).

Table 1

Geometrical and electrical parameters of the finite element model.

	Geometrical Parameters: *Nerve*			*mm unless otherwise indicated*
Height	**Radii**			
	Medium	**Epineurium/nerve**	**Endoneurium/fascicle**	
100	20	1.5 [28]	Randomly chosen from truncated Gaussian distribution: μ = 0.225σ = 0.0625constrained to μ ± 2σ [29]	
	Geometrical Parameters: *Cuff Electrode*			*mm unless otherwise indicated*
	Height	Radius	Thickness	Subtending angle (deg.)
Silicone rubber [30,31]	10.8	3.2	2.2	63
Active electrode [30,31]	2.8	3.2	N/A	83
Encapsulation tissue[a] [32,33]	N/A	N/A	0.15	N/A
	Electrical Parameters			*Ω-m unless otherwise indicated*
Medium	**Encapsulation tissue**	**Epineurium**	**Perineurium**	**Endoneurium**
30 [34]	6.3 [35]	6.3 [35,36]	0.05 Ω-m^2 [37]	1.75 longitudinal 6.00 radial[b] [25]

[a] We allowed 75 μm of the extraneural fatty medium between the nerve and the encapsulation tissue to prevent a singularity when assembling and meshing the geometry.

[b] Halved from [25]. See text for details.